RESEARCH ARTICLE

NANO · MICRO small
www.small-journal.com

Fabrication of Single-Crystal Violet Phosphorus Flakes For Ultrasensitive Photodetection

Yumin Da, Yongheng Zhou, Shuai Zhang, Yang Li, Tongtong Jiang, Wenting Zhu, Paul K. Chu, Xue-Feng Yu, Xiaolong Chen, and Jiahong Wang**

Violet phosphorus (VP) has attracted a lot of attention for its unique physicochemical properties and emerging potential in photoelectronic applications. Although VP has a van der Waals (vdW) structure similar to that of other 2D semiconductors, direct synthesis of VP on a substrate is still challenging. Moreover, optoelectronic devices composed of transfer-free VP flakes have not been demonstrated. Herein, a bismuth-assisted vapor phase transport technique is designed to grow uniform single-crystal VP flakes on the SiO_2/Si substrate directly. The size of the crystalline VP flakes is an order of magnitude larger than that of previous liquid-exfoliated samples. The photodetector fabricated with the VP flakes shows a high responsivity of 12.5 A W^{-1} and response/recovery time of 3.82/3.03 ms upon exposure to 532 nm light. Furthermore, the photodetector shows a small dark current (<1 pA) that is beneficial to high-sensitivity photodetection. As a result, the detectivity is 1.38×10^{13} Jones that is comparable with that of the vdW *p–n* heterojunction detector. The results reveal the great potential of VP in optoelectronic devices as well as the CVT technique for the growth of single-crystal semiconductor thin films.

1. Introduction

Violet phosphorus (VP) is an emerging 2D semiconductor with high air stability and unique optoelectronic features.[1,2] Since the atomic structure of VP was determined by Zhang et. al. in 2020, many attempts have been made to synthesize bulk VP crystals and exfoliate them into nanosheets for electronic devices.[3,4] Among the various exfoliation methods, liquid sonication is a common approach for VP nanosheets[5,6] and different liquid-exfoliated VP-based field-effect transistors (FETs) show mobility of ≈0.05 $cm^2/(V{\cdot}s)$ or 2.25 $cm^2/(V{\cdot}s)$.[7,8] Unfortunately, liquid exfoliation only produces materials on a small scale and the products have an irregular shape and low crystallinity.[7,9,10] More importantly, the surface and edge defects resulting from liquid exfoliation seriously compromise the performance of VP-based devices.[7,11,12] In comparison, mechanical exfoliation is effective in the synthesis of 2D materials.[13,14] However, mechanical-exfoliated VP flakes tend to have an uneven surface and rough edges, which hinder subsequent processing of optoelectronic devices.[15–17] Hence, direct growth of thin VP flakes on a substrate is crucial to the development of advanced VP-based microelectronics devices.

Chemical vapor deposition (CVD) is a popular technique to synthesize 2D vdW materials on insulating or conductive substrates, and various 2D materials including graphene, MoS_2, WSe_2, $MoTe_2$, BN, and so on have been deposited.[18–22] However, up to now, all the phosphorus films deposited on insulating substrates are amorphous red phosphorus, and few nanocrystalline phosphorus allotropes grown on insulating SiO_2 have the nanorod or micronoodle morphology, consequently making the determination of the intrinsic properties of individual nanocrystals difficult.[23] Efforts have been made on the chemical vapor transport (CVT) growth of phosphorus allotropes and metal species have been shown to reduce the nucleation and diffusion barriers of 2D materials.[24,25] Therefore, metal-assisted CVT has been applied to the fabrication of nanoflakes of 2D phosphorus allotropes.[26,27] For example, large-scale bottom-up synthesis of crystalline black phosphorus (BP) and fibrous phosphorus films on the SiO_2/Si substrate in the presence of tin and iodine has been reported.[28] However, the bottom-up synthesis of large and regular single-crystal VP flakes is still prone to delivering unreliable results thereby hampering the development of VP-based optoelectronic devices.

Herein, a bismuth-assisted vapor phase transport (CVT) technique is designed to synthesize single-crystal VP flakes with the

Y. Da, S. Zhang, Y. Li, T. Jiang, W. Zhu
Shenzhen Institute of Advanced Technology
Chinese Academy of Sciences
Shenzhen 518055, P. R. China
Y. Da, X.-F. Yu, J. Wang
University of Chinese Academy of Sciences
Beijing 100049, P. R. China
E-mail: jh.wang1@siat.ac.cn
Y. Zhou, X. Chen
Department of Electrical and Electronic Engineering
Southern University of Science and Technology
1088 Xueyuan Avenue, Shenzhen 518055, P. R. China
E-mail: chenxl@sustech.edu.cn
P. K. Chu
Department of Physics
Department of Materials Science and Engineering
and Department of Biomedical Engineering
City University of Hong Kong
Tat Chee Avenue, Kowloon, Hong Kong P. R. China

The ORCID identification number(s) for the author(s) of this article can be found under https://doi.org/10.1002/smll.202310276

DOI: 10.1002/smll.202310276

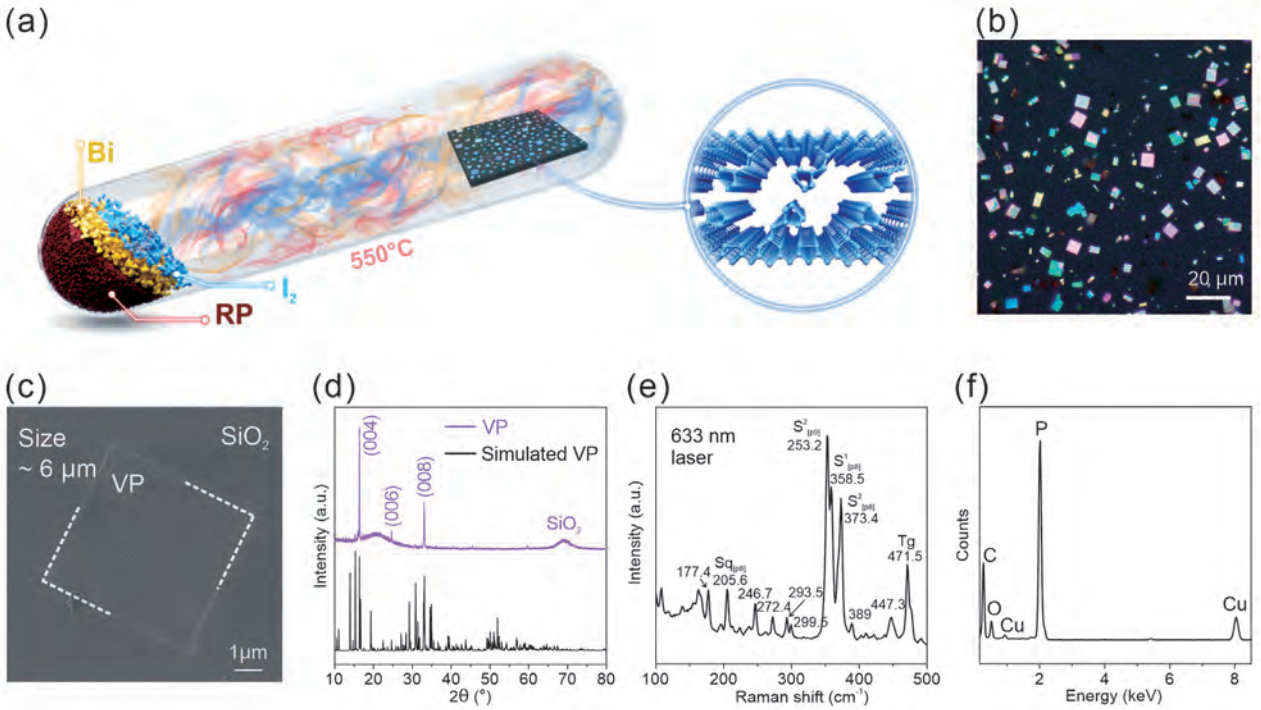

Figure 1. Characterization of VP flakes prepared on the SiO_2/Si substrate: a) Schematic diagram showing the direct growth of VP on SiO_2/Si; b) Bright-field optical microscopy image of VP on the substrate; c) SEM image of a typical individual VP flake with a regular morphology; d) XRD pattern of the VP flake grown on the SiO_2/Si substrate and simulated VP; e) Raman scattering spectrum of the VP flake grown on SiO_2/Si excited by the 633 nm laser; f) EDS spectrum of the VP flake on the copper grid.

regular quadrilateral morphology directly in a large area (exceeding 100 μm^2) on the silica/silicon (SiO_2/Si) substrate. To demonstrate the practical potential, the VP flakes are used to fabricate a photodetector with a wide photoresponsive range spanning the visible to near-infrared regimes. When V_{ds} is set to 5 V, the responsivity reaches 12.5 A W^{-1} in the visible light spectra. Moreover, the VP-based photodetector shows better detectivity, current noise spectral density, and noise equivalent power (NEP) than many transition-metal dichalcogenides (TMDCs) or heterojunction photodetectors.

2. Results and Discussion

2.1. Direct Growth of VP on SiO2/Si

Figure 1a schematically illustrates the one-step bismuth-assisted CVT approach for the direct growth of VP flakes on SiO_2/Si. The reactants including amorphous red phosphorus, bismuth, iodine, and insulating SiO_2/Si substrate are sealed together in a vacuum quartz tube. As the temperature of the muffle decreases from 550 to 300 °C, the crystalline VP flakes are formed on SiO_2/Si without complicated separation and transfer processes. During the growth, the evaporated phosphorus species are transformed into amorphous red phosphorus trans of bismuth and iodine and thus effectively promote nucleation and growth of VP on the SiO_2/Si substrate. As shown in Figure 1b, the VP flakes are regular rectangles or squares and some flakes are larger than 100 μm^2. The statistical analysis demonstrates that the side length of VP is 6–10 μm (Figure S1, Supporting Information), which is much larger than that of previously reported exfoliated VP flakes. The scanning electron microscopy (SEM) image of an individual crystalline VP flake have a diameter of ≈6 μm (Figure 1c). Atomic force microscopy (AFM) shows that the thicknesses of the thinner VP flakes are 21 and 32 nm, respectively and the smooth AFM profile indicates a glossy surface morphology for the VP flakes (Figure S2a,b, Supporting Information). As the size of the VP flakes increases, the thickness goes up as well and therefore, VP flakes with a size of ten micrometers can be prepared when the thickness is a hundred nanometers (Figure S2c,d, Supporting Information). The AFM height statistics of as-grown VP flakes shows their thickness ranges from 20 to 180 nm, in which the 80% thicknesses of VP flakes are less than 100 nm (Figure S2e, Supporting Information). The X-ray diffraction (XRD) patterns of the as-grown VP flakes and simulated diffraction peaks are exhibited in Figure 1d. Owing to the preferred orientation of the nucleation process, there are conspicuous diffraction peaks at 16.4°, 24.6°, and 33.0° corresponding to the (004), (006), and (008) planes of VP, respectively. The sharp and intense XRD diffraction peaks suggest that the VP flakes have high crystallinity. Since the monoclinic VP consists of unique bi-tubular low symmetrical units, the vibration modes produce characteristic Raman scattering signals. As shown in Figure 1e, the Raman peaks at 205.6, 253.2, 358.5, 373.4, and 471.5 cm^{-1} are assigned to $Sq_{[p8]}$, $S^2_{[P9]}$, $S^1_{[p8]}$, $S^2_{[p8]}$, and Tg, respectively, which are in agreement with the Raman spectrum of the VP single crystal,[3] thus verifying that the CVT approach can produce high-quality VP flakes directly on the substrate. Energy-dispersive X-ray spectrometer (EDS) further confirms the high purity (Figure 1f).

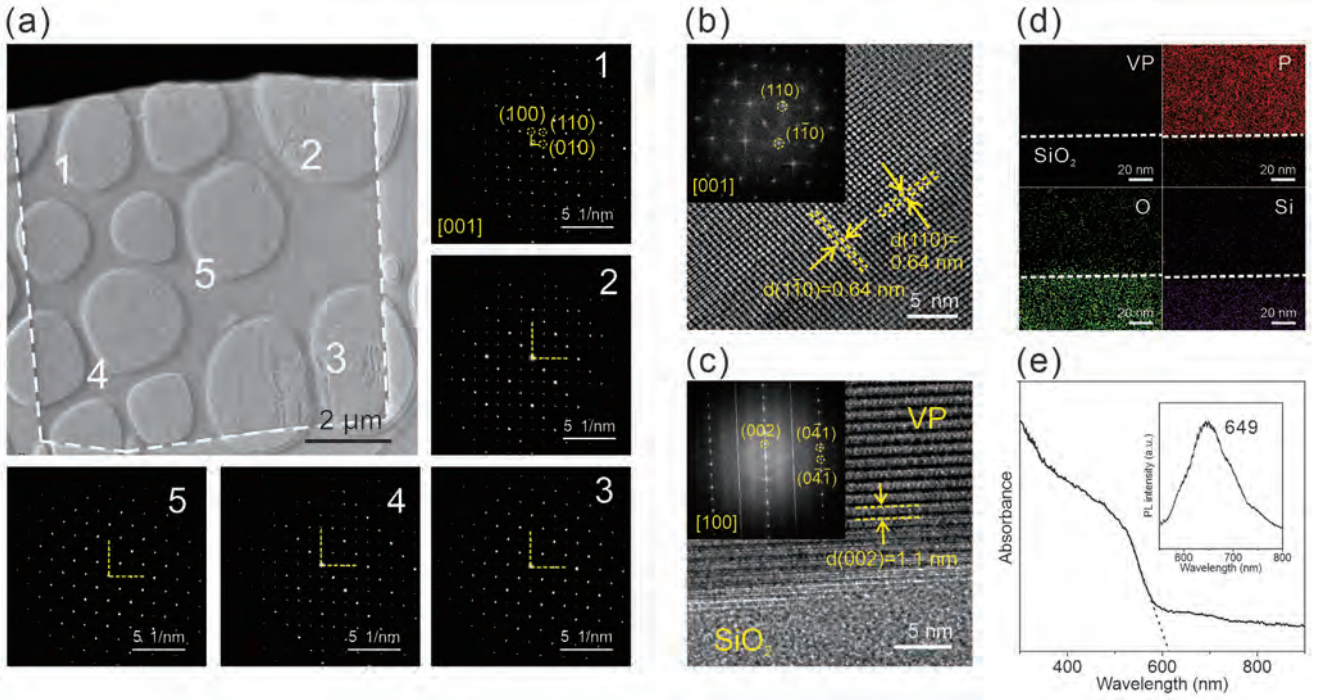

Figure 2. Atomic structure and optical features of the VP flakes: a) Low-magnification TEM image of the VP flakes and SAED patterns acquired from five regions indicated in the TEM image, revealing that the VP flakes are single crystalline; b) HR-TEM image of the VP flakes with the inset showing the Fourier transform pattern; c) Cross-sectional HR-TEM image of the interface between the VP flakes and SiO_2/Si substrate with the inset showing the Fourier transform pattern; d) Cross-sectional HAADF-STEM image of and corresponding P, O, and Si elemental maps in the interface between the VP flakes and SiO_2/Si substrate; e) UV–vis–NIR absorption and PL spectra of VP flakes.

2.2. Structure of VP Flakes

To determine the crystalline structure, the VP flakes are detached integrally from the SiO_2/Si substrate with the aid of a water-soluble polyvinyl alcohol mediator and examined by transmission electron microscopy (TEM) using a copper grid. The representative low-magnification TEM image of an individual VP flake is depicted in **Figure** 2a and the quasi-square morphology is consistent with the OM and SEM images. The selected-area electron diffraction (SAED) patterns acquired from five different locations indicate high crystallinity. In the SAED pattern, diffraction dots corresponding to the (100), (110), and (010) planes are observed in all the areas. Moreover, all five SAED patterns exhibit consistent orientations confirming the single-crystal characteristics. The high-resolution TEM (HR-TEM) image (Figure 2b) discloses a uniform lattice spacing of 6.4 Å assigned to the (110) and (1-10) lattice planes of VP, which is verified by the Fourier transform pattern in the inset.

To further analyze the interface, the VP flake on SiO_2/Si is cut by a focused ion beam (FIB), and the cross-section is examined by TEM as shown in Figure 2c. A sharp interface is observed between the clear stacked lamellar structure of VP and amorphous SiO_2, and the interlayer distance is 1.1 nm. The inset shows the Fourier transform pattern that corroborates the (002) facet of VP. The high-angle annular dark-field imaging (HAADF) scanning TEM (STEM) image and EDS maps in Figure 2d demonstrate the distinct spatial boundary between phosphorus and the silica substrate. In addition, two key factors are required for the growth of VP: 1) the suitable P_4 partial pressure in synthesis temperature; 2) producing P–Bi–I composites to promote VP nucleation during the CVT reaction because the transportation conditions for VP synthesis is similar to that for black phosphorus (BP).[26] If mineralizers are absent, the RP is found on the surface of the SiO_2/Si substrate after the CVT reaction (Figure S3a,b, Supporting Information) as verified by Raman scattering (Figure S3c, Supporting Information). Thus, only iodine does not facilitate nucleation of VP and serves as a CVT transport agent. The small amounts of mineralizer (Bi) could produce P–Bi–I gaseous composites during 550 °C synthesis temperature, and these compounds system are crucial to facilitate heterogeneous nucleation of VP flakes onto silicon.[29] Based on the effective spatial catalytic process, the nucleation and growth of VP on the insulating substrate are realized with the assistance of Bi and I_2. The UV–vis–NIR absorption and photoluminescence (PL) spectra reveal the optical features of the VP flakes (Figure 2e). The broad absorption band indicates an optical bandgap (E_g) of 1.87 eV and the excitonic transitions from VP appear at ≈1.9 eV (650 nm) matching approximately the UV–vis–NIR absorption edge.

2.3. Properties of the VP Flake-Based Photodetector

Owing to the large illumination area and configurated charge carriers transport route, 2D semiconductors have been developed for various photodetectors.[30–32] Most detectors are stimulated by

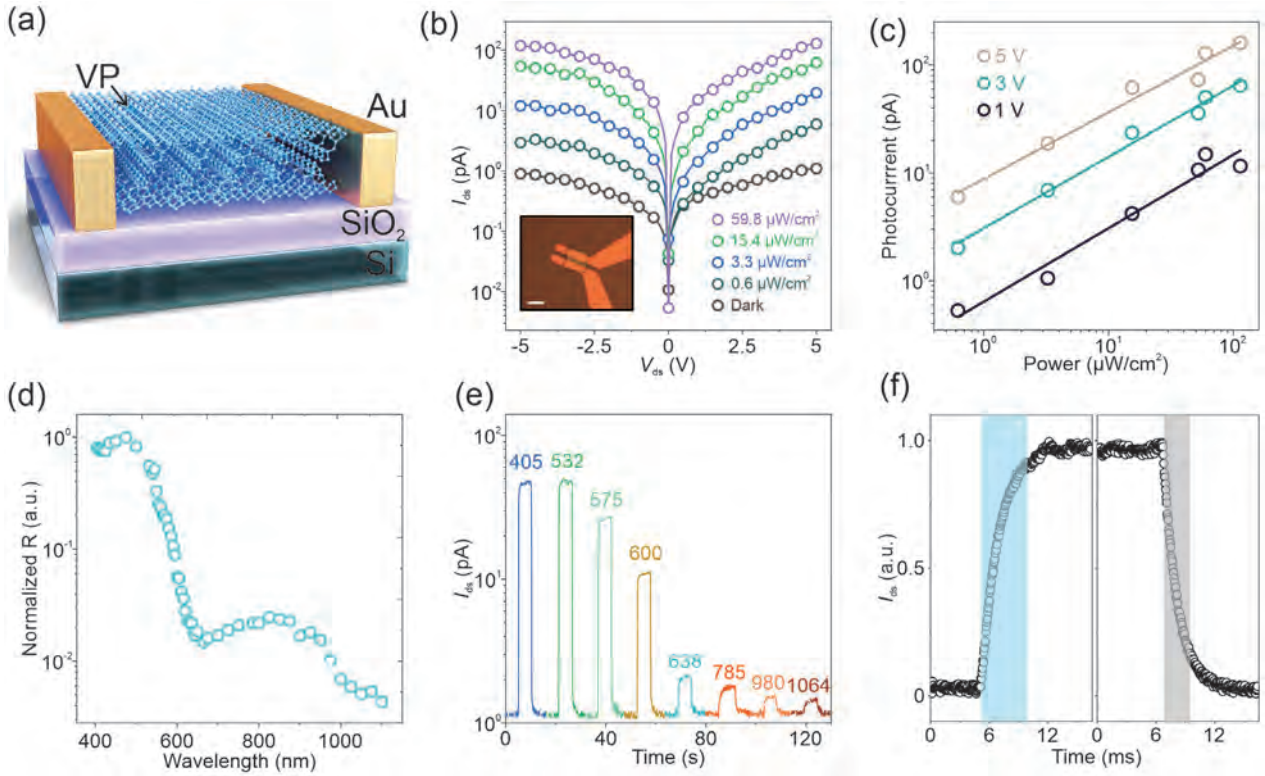

Figure 3. a) 3D schematic of the VP photodetector; b) $I_{ds}-V_{ds}$ curves of the VP photodetector for different illumination powers at a wavelength of 532 nm with the inset showing the optical image of the VP photodetector (scale bar is 10 μm); c) Power dependence of the photocurrents for different V_{ds} with the effective area of the VP device being 2.1×10^{-7} cm^2; d) Normalized responsivity of the VP photodetector as a function of wavelength; e) Total currents I_{ds} as a function of time for different illumination wavelengths (power density of 0.47 mW cm^{-2} and V_{ds} of 2 V); f) Response and recovery times of the VP photodetector.

high-power lasers (>100 mW cm^{-2}),[33] but the safe threshold for human eyes is less than 10 mW cm^{-2}. Therefore, photodetectors should be designed to work with low light stimulation in practice, and some complex heterostructure channels or diverse device structures have been proposed.[34,35] From the perspective of cost and easy operation, semiconductor-based low-light photodetectors are desirable. Here, VP photodetectors are fabricated on SiO_2/Si with a 285 nm-thick SiO_2 layer (See Experimental Section). **Figure** 3a presents the schematic of the VP photodetector comprising Au electrodes. Figure 3b shows the optical image and $I_{ds}-V_{ds}$ curves of the VP photodetector for different illumination power. The thickness of VP is 25 nm determined by AFM. A very low dark current (<1 pA) is observed boding well for highly-sensitive photodetection. The device shows excellent characteristics at a large drain-source bias V_{ds}. For example, the dark current at 5 V is ≈3 times higher than that at 1 V, while the photocurrent (at an incident light power density of 60 μW cm^{-2}) shows an 8-fold enhancement.

Figure 3c shows the power-dependent photocurrents for different V_{ds}. The correlation between the photocurrents and light power density can be described by $I_p = aP^b$, where I_p is the photocurrent, P is the light power density, and a and b are constants. For V_{ds} of 1, 3, and 5 V, the b values are 0.47 ± 0.19, 0.57 ± 0.08 and 0.58 ± 0.13, respectively. Here, the non-unity exponent ($0 < b < 1$) indicates that some photocarriers may be trapped by defect states in VP.[36] According to previous reports, the bandgap of bulk VP is 2 eV (620 nm),[3] implying that the VP photodetector is suitable for visible light applications. In order to its detection range, the responsivity of the device for various excitation wavelengths is studied. The incident light comes from a halogen lamp instead of lasers. The responsivity is calculated by $R = I_p/P$and shown in Figure 3d. The device shows high responsivity above 620 nm with a maximum value at 475 nm and the results are consistent with the measured absorption and PL spectra. The VP photodetector also shows photoresponse to near-infrared light as shown in Figure 3d,e. The photoresponse to the near-infrared light does not originate from electron transitions from the intrinsic bandgap, since it is unlikely that the low power of the incident light (≈85 pW) produces the two-photon absorption effect. On the other hand, both photolithography and metal deposition may affect the surface of VP and produce defect states (such as oxidation and vacancies) in VP.[37] These defect states may introduce an additional in-gap energy level, which allows the photoresponse to near-infrared light. Hence, the response rate is studied. Here, the response and recovery time are defined as the duration for photocurrent to rise/fall from 10%/90% to 90%/10% of the maximum value. As shown in Figure 3f, the response and recovery times of the VP photodetector are 3.82 and 3.03 ms, respectively and a faster response rate is expected with further optimization of the defect states. In addition, the as-prepared VP photodetector shows a great stable photoelectric performance in vacuum (Figure S5a, Supporting Information),

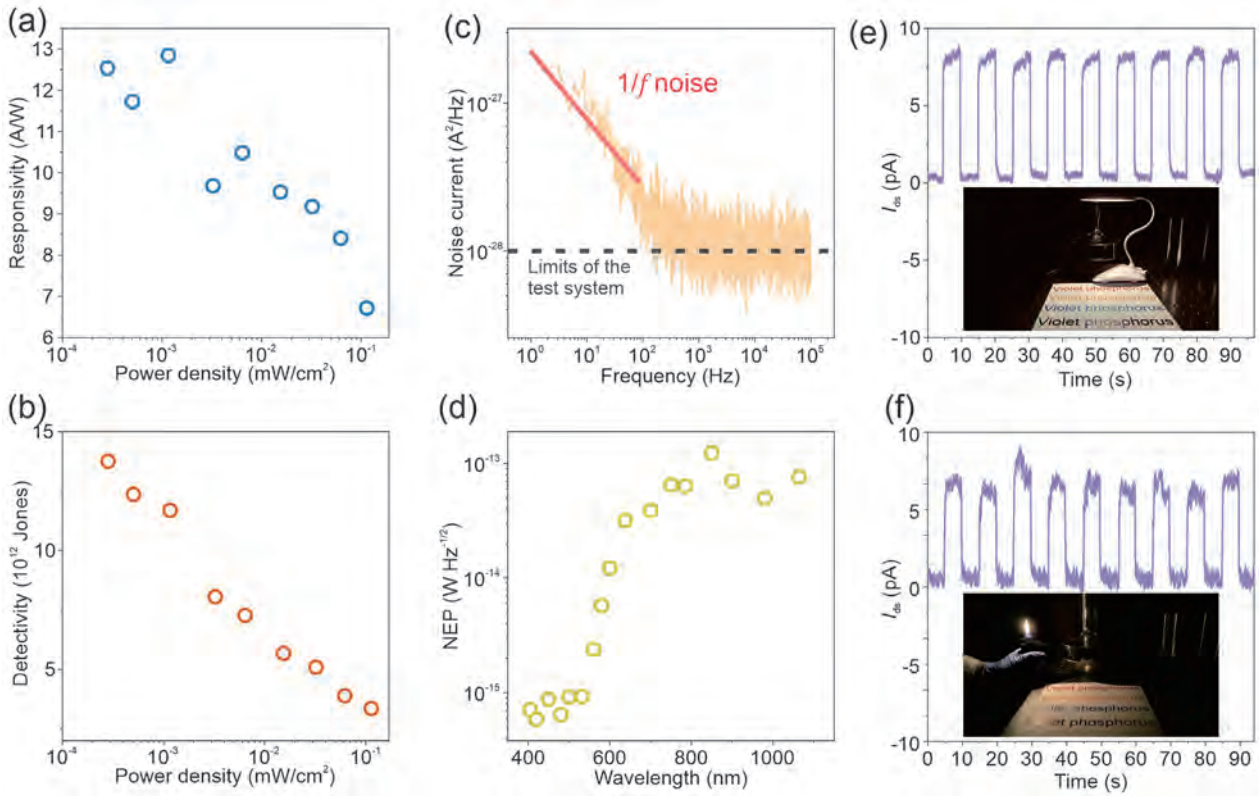

Figure 4. a) Power-dependent responsivity and b) Specific detectivity; c) Noise of the VP photodetector with the red dashed line serving as the guideline for 1/*f* noise and black dashed line showing the lowest noise level ($\approx 10^{-28}$ A^2 Hz^{-1}) limited by our measurement system; d) Noise equivalent power as a function of wavelength from visible to near-infrared; e,f) Total current of the VP photodetector illuminated by e) LED and f) Lighter (f), respectively, as a bias voltage of 1 V.

nevertheless, it is unstable photocurrent performance in atmosphere condition. Therefore, we introduced boron nitride (hBN) on the VP surface to verify the stability of VP-based photoelectric device in atmosphere condition. The VP/hBN photodetector exhibit a good stable photoelectric performance for three days (Figure S5b,d, Supporting Information), suggesting that VP-based photodetector enables to obtain a good stability in atmosphere condition.

Figure 4a shows the power dependence of the responsivity under weak 532 nm light exposure. The maximum responsivity is 12.5 A W^{-1} at V_{ds} = 5 V when the light power density is only 0.3 μW cm^{-2}.[38] If we only consider the shot noise in the device, the specific detectivity can be calculated by $D_C^* = RA^{1/2}/(2eI_d)^{1/2}$, where I_d is the dark current, and A is the effective photosensitive region of the device. Here, the detectivity is the calculated detectivity (D_C^*) and the VP photodetector shows an impressive D_C^* of 1.38×10^{13} Jones (Figure 4b), which is comparable to or higher than those of many TMDCs-based photodetectors for the same wavelength range (Table S1, Supporting Information). Since the shot noise is not the only noise component, the magnitude of the noise current is usually underestimated thus leading to overestimated detectivity. Hence, the current noise spectral density is determined. As shown in Figure 4c, there is a flicker (1/*f*) noise (red dashed line) in the low-frequency region (below 10^2 Hz). The noise reaches a minimum of $\approx 10^{-28}$ A^2 Hz^{-1} (limited by the sensitivity of our equipment) when the frequency is above 10^3 Hz. The measured specific detectivity (D_M^*) based on the measured noise current is calculated to be $\approx 6.4 \times 10^{11}$ Jones at 405 nm (Figure S4 and Table S1, Supporting Information). It is noted that this value is the lower limit of the photodetector, because the measured noise current is limited by the sensitivity of our equipment. The noise equivalent power (NEP) is another important parameter that can be calculated by $NEP = RMS(I_n)/R$, where $RMS(I_n)$ is the root-mean-square noise with a value of 1.05×10^{-14} A Hz$^{-1/2}$. As shown in Figure 4d, the NEP shows a minimum value of 5.83×10^{-16} W Hz$^{-1/2}$ at 420 nm, which is comparable to those of other van der Waals (vdW) *p*–*n* heterostructures.[39–41] The properties of our VP-flake photodetector are compared to those of previously reported VP-based devices in Table S2 (Supporting Information). The outstanding responsivity and detectivity performance of our VP photodetector attributes to the high-crystalline morphology of the VP flakes. To further demonstrate the high sensitivity, weak incident light from commercial LEDs and lighters is used, and as shown in Figure 4e,f, the photodetector shows clear photoresponse and high sensitivity in spite of low-light exposure.

3. Conclusion

Direct growth of large-size single-crystal VP flakes is accomplished on the insulating SiO_2/Si substrate by a bismuth-assisted CVT technique. The size of the single-crystal VP flakes

exceeds tens of micrometers. The photodetector fabricated without a transfer process shows higher responsivity and faster response/recovery than other VP photodetectors reported so far. The VP photodetector shows an impressive detectivity D_C^* of 1.38×10^{13} Jones under 0.3 μW cm^{-2} irradiation, which is superior to that of many other 2D materials photodetectors. Upon illumination by weak light from commercial LEDs or lighters, the photodetector still shows a clear photoresponse. These results reveal a new technique for the bottom-up production of single-crystal VP flakes that have large potential in optoelectronic applications.

4. Experimental Section

VP Flakes Growth: Red phosphorus (Western Elements, 99.999%), tin particles (Aldrich, 99.9%), iodine (Aldrich, 99.99%), and 275 nm SiO_2/Si wafers were purchased from commercial suppliers. The SiO_2/Si substrates were treated with alcohol, acetone, and ultra-pure water before growth. The red P, Bi, I_2, and SiO_2/Si substrates were enclosed in evacuated silica glass tubes as precursors. The sealed quartz tube was placed in a muffle furnace horizontally with the raw materials, in which the SiO_2 side was placed horizontally upward. The temperature was raised from room temperature to 550 °C and after keeping at 550 °C for 75 min, the temperature was slowly reduced to 300 °C in 1000 min. The product cooled slowly to room temperature for 300 min.

Preparation of Cross-Sectioned TEM Samples: A 70 nm Au–Pd film was deposited on the VP sample by thermal evaporation to protect the sample and Pt was sputter-deposited on the dual beam instrument (FEI Nova NanoLab 600). Using a 5 KV Ga^+ beam, trenches were milled around the Pt strap. The cross-sectioned VP sample was extracted and transferred to a copper grid.

Materials Characterization: The morphology of the VP flakes was examined by scanning electron microscopy (SEM, Zeiss GeminiSEM 300) and optical microscopy (OM, ZEISS Primotech). XRD was performed on the Rigaku Smartlab 3 kW X-ray diffractometer with Cu K_α radiation (λ = 1.54056 Å, 40 kV, 30 mA, 10° min^{-1} from 10° to 80°). The TEM images, high-resolution TEM images, HAADF images, and EDS spectra were acquired on the Tecnai G2 F20 S-Twin at an acceleration voltage of 300 kV. Raman scattering was carried out on the Horiba Jobin Yvon LabRam HR-VIS high-resolution confocal Raman microscope equipped with a 633 nm laser. AFM was performed on the Cypher S AFM (Asylum Research, USA) in the tapping mode and the electron paramagnetic resonance spectra were acquired from the German Brucker EMX-10/12. The PL were obtained by fluorescent spectrophotometry (Hitachi F-4600 and Edinburgh FLS-1000) and the UV–vis absorption spectra were collected on the UV–vis spectrophotometer (UV-1800, Shimadzu).

Preparation of VP/hBN: The VP/hBN was prepared though PVA-assisted dry transfer method. The polyvinyl alcohol (PVA, Sigma–Aldrich, 80% hydrolyzed, 9000–10 000 molecular weight) powder was dissolved in deionized water with a mass ratio of 10%. First, the PVA film was spin-coated on a clean SiO_2/Si substrate, where a thin hBN flake was further exfoliated on top. Then the PVA film with hBN was peeled off from the substrate and transferred on the top of VP photodetector in glove box, leading to the formation of VP/hBN. Finnaly, the PVA film was dissolved in deionized water.

Device Fabrication and Photocurrent Measurements: The VP-based photodetectors were fabricated by standard photolithography (MicroWriter ML3, Durham Magneto Optics Ltd). To fabricate the electrodes, 5 nm Cr and 75 nm Au thin films were deposited onto the patterned samples by thermal evaporation followed by the lift-off process in acetone. The devices were characterized by a semiconductor parameter analyzer (FS-Pro) under vacuum (≈10^{-6} mbar) in a probe station (Advanced Research System). The monochromatic halogen lamp (Omni-λ–300 Zolix) was the light source.

Supporting Information

Supporting Information is available from the Wiley Online Library or from the author.

Acknowledgements

Y.D. and Y.Z. contributed equally to this work. The authors acknowledge the financial support from the National Natural Science Foundation of China (21975280, 32101197, and 62275117), Youth Innovation Promotion Association Chinese Academy of Sciences (2020354), Shenzhen Science and Technology Program (JCYJ20220818100806014), Shenzhen Excellent Youth Program (RCYX 20221008092900001), City University of Hong Kong Donation Research Grants (DON-RMG 9229021 and 9220061), City University of Hong Kong Strategic Research Grant (SRG No. 7005505), and Guangdong Major Talent Project (2019QN01C177). The authors thank Prof. Jun Liu of South China University of Technology for the FIB assistance.

Conflict of Interest

The authors declare no conflict of interest.

Data Availability Statement

The data that support the findings of this study are available from the corresponding author upon reasonable request.

Keywords

2D materials, chemical vapor transport, low light photodetector, violet phosphorus

Received: November 10, 2023
Revised: January 19, 2024
Published online: March 3, 2024

[1] G. Schusteritsch, M. Uhrin, C. J. Pickard, *Nano Lett.* **2016**, *16*, 2975.
[2] Y. L. Lu, S. Dong, W. Zhou, S. Dai, B. Zhou, H. Zhao, P. Wu, *Phys. Chem. Chem. Phys.* **2018**, *20*, 11967.
[3] L. Zhang, H. Huang, B. Zhang, M. Gu, D. Zhao, X. Zhao, L. Li, J. Zhou, K. Wu, Y. Cheng, J. Zhang, *Angew. Chem., Int. Ed.* **2020**, *132*, 1090.
[4] X. Liu, S. Wang, Z. Di, H. Wu, C. Liu, P. Zhou, *Adv. Sci.* **2023**, *10*, 2301851.
[5] L. Zhang, X. Li, F. Yao, L. Li, H. Huang, X. Zhao, S. Liu, Y. Cheng, H. Xu, J. Zhang, *Adv. Funct. Mater.* **2022**, *32*, 1.
[6] L. Zhang, H. Huang, Z. Lv, L. Li, M. Gu, X. Zhao, B. Zhang, Y. Cheng, J. Zhang, *ACS Appl. Electron. Mater.* **2021**, *3*, 1043.
[7] S. Lin, W. K. Lai, Y. Li, W. Lu, G. Bai, S. P. Lau, *SmartMat* **2021**, *2*, 226.
[8] A. G. Ricciardulli, Y. Wang, S. Yang, P. Samorì, *J. Am. Chem. Soc.* **2022**, *144*, 3660.
[9] V. Nicolosi, M. Chhowalla, M. G. Kanatzidis, M. S. Strano, J. N. Coleman, *Science* **2013**, *340*, 72.
[10] N. M. Latiff, C. C. Mayorga-Martinez, Z. Sofer, A. C. Fisher, M. Pumera, *Appl. Mater. Today* **2018**, *13*, 310.
[11] B. Zhang, Z. Wang, H. Huang, L. Zhang, M. Gu, Y. Cheng, K. Wu, J. Zhou, J. Zhang, *J. Mater. Chem. A* **2020**, *8*, 8586.
[12] F. Baumer, Y. Ma, C. Shen, A. Zhang, L. Chen, Y. Liu, D. Pfister, T. Nilges, C. Zhou, *ACS Nano* **2017**, *11*, 4105.

[13] Y. Huang, Y. H. Pan, R. Yang, L. H. Bao, L. Meng, H. L. Luo, Y. Q. Cai, G. D. Liu, W. J. Zhao, Z. Zhou, L. M. Wu, Z. L. Zhu, M. Huang, L. W. Liu, L. Liu, P. Cheng, K. H. Wu, S. B. Tian, C. Z. Gu, Y. G. Shi, Y. F. Guo, Z. G. Cheng, J. P. Hu, L. Zhao, G. H. Yang, E. Sutter, P. Sutter, Y. L. Wang, W. Ji, X. J. Zhou, et al., *Nat. Commun.* **2020**, *11*, 2453.
[14] M. Yi, Z. Shen, *J. Mater. Chem. A* **2015**, *3*, 11700.
[15] B. Zhang, E. Martel, Z. Wang, J. Zhang, T. Szkopek, *Nanotechnology* **2023**, *34*, 285206.
[16] H. Wang, S. Liu, P. Wang, H. Ge, Y. Chen, H. Wang, T. Xu, J. Guo, Y. Zou, W. Wei, R. Jiang, F. Wang, P. Martyniuk, J. Miao, W. Hu, *Sci. China Physics, Mech. Astron.* **2023**, *66*, 297311.
[17] Y. Li, S. Cai, W. K. Lai, C. Wang, L. Rogée, L. Zhuang, L. Zhai, S. Lin, M. Li, S. P. Lau, *Adv. Opt. Mater.* **2022**, *10*, 2101538.
[18] J. Du, B. Tong, S. Yuan, N. Dai, R. Liu, D. Zhang, H. M. Cheng, W. Ren, *Adv. Funct. Mater.* **2022**, *32*, 2203115.
[19] J. Hu, F. Zhou, J. Wang, F. Cui, W. Quan, Y. Zhang, *Adv. Funct. Mater.* **2023**, *33*, 2303520.
[20] X. Jia, Z. Cheng, B. Han, X. Cheng, Q. Wang, Y. Ran, W. Xu, Y. Li, P. Gao, L. Dai, *Small* **2023**, *19*, 2207927.
[21] P. Yang, J. Zha, G. Gao, L. Zheng, H. Huang, Y. Xia, S. Xu, T. Xiong, Z. Zhang, Z. Yang, Y. Chen, D. K. Ki, J. J. Liou, W. Liao, C. Tan, *Nano-Micro Lett.* **2022**, *14*, 109.
[22] S. Bhowmik, A. Govind Rajan, *iScience* **2022**, *25*, 103832.
[23] P. E. M. Amaral, G. P. Nieman, G. R. Schwenk, H. Jing, R. Zhang, E. B. Cerkez, D. Strongin, H. F. Ji, *Angew. Chem., Int. Ed.* **2019**, *58*, 6766.
[24] L. Tan, M. Zeng, Q. Wu, L. Chen, J. Wang, T. Zhang, J. Eckert, M. H. Rümmeli, L. Fu, *Small* **2015**, *11*, 1840.
[25] H. Wang, G. Yu, *Adv. Mater.* **2016**, *28*, 4956.
[26] L. Zhang, M. Gu, L. Li, X. Zhao, C. Fu, T. Liu, X. Xu, Y. Cheng, J. Zhang, *Chem. Mater.* **2020**, *32*, 7363.
[27] Y. Zeng, Z. Guo, *iScience* **2021**, *24*, 103116.
[28] Y. Xu, X. Shi, Y. Zhang, H. Zhang, Q. Zhang, Z. Huang, X. Xu, J. Guo, H. Zhang, L. Sun, Z. Zeng, A. Pan, K. Zhang, *Nat. Commun.* **2020**, *11*, 1330.
[29] Z. Sun, W. Chen, B. Zhang, L. Gao, K. Tao, Q. Li, J. L. Sun, Q. Yan, *Nat. Commun.* **2023**, *14*, 1.
[30] J. Zha, M. Luo, M. Ye, T. Ahmed, X. Yu, D. H. Lien, Q. He, D. Lei, J. C. Ho, J. Bullock, K. B. Crozier, C. Tan, *Adv. Funct. Mater.* **2022**, *32*, 2111970.
[31] P. V. Pham, S. C. Bodepudi, K. Shehzad, Y. Liu, Y. Xu, B. Yu, X. Duan, *Chem. Rev.* **2022**, *122*, 6514.
[32] G. Liu, Z. Sun, J. Su, X. Feng, Q. Peng, H. Li, T. Zhai, *Chinese Sci. Bull.* **2021**, *66*, 4036.
[33] W. Liu, Y. Yu, M. Peng, Z. Zheng, P. Jian, Y. Wang, Y. Zou, Y. Zhao, F. Wang, F. Wu, C. Chen, J. Dai, P. Wang, W. Hu, *InfoMat* **2023**, *5*, e12470.
[34] W. Ahmad, L. Pan, K. Khan, L. Jia, Q. Zhuang, Z. Wang, *Adv. Funct. Mater.* **2023**, *33*, 2300686.
[35] L. Pi, P. Wang, S. J. Liang, P. Luo, H. Wang, D. Li, Z. Li, P. Chen, X. Zhou, F. Miao, T. Zhai, *Nat. Electron.* **2022**, *5*, 248.
[36] H. Fang, W. Hu, *Adv. Sci.* **2017**, *4*, 1700323.
[37] G. He, T. Dong, Z. Yang, P. Ohlckers, *Chem. Mater.* **2019**, *31*, 9917.
[38] K. K. Manga, J. Wang, M. Lin, J. Zhang, M. Nesladek, V. Nalla, W. Ji, K. P. Loh, *Adv. Mater.* **2012**, *24*, 1697.
[39] H. J. Kwon, H. Kang, J. Jang, S. Kim, C. P. Grigoropoulos, *Appl. Phys. Lett.* **2014**, *104*, 083110.
[40] J. Renteria, R. Samnakay, S. L. Rumyantsev, C. Jiang, P. Goli, M. S. Shur, A. A. Balandin, *Appl. Phys. Lett.* **2014**, *104*, 153104.
[41] W. C. Tan, L. Huang, R. J. Ng, L. Wang, D. M. N. Hasan, T. J. Duffin, K. S. Kumar, C. A. Nijhuis, C. Lee, K. W. Ang, *Adv. Mater.* **2018**, *30*, 1705039.

NANO · MICRO small

Supporting Information

for *Small*, DOI 10.1002/smll.202310276

Fabrication of Single-Crystal Violet Phosphorus Flakes For Ultrasensitive Photodetection

Yumin Da, Yongheng Zhou, Shuai Zhang, Yang Li, Tongtong Jiang, Wenting Zhu, Paul K. Chu, Xue-Feng Yu, Xiaolong Chen and Jiahong Wang**

Supporting Information

69451 Weinheim, Germany

Fabrication of single-crystal violet phosphorus flakes for ultrasensitive photodetection

Yumin Da[#], Yongheng Zhou[#], Shuai Zhang, Yang Li, Tongtong Jiang, Wenting Zhu, Paul K. Chu, Xue-Feng Yu, Xiaolong Chen, Jiahong Wang**

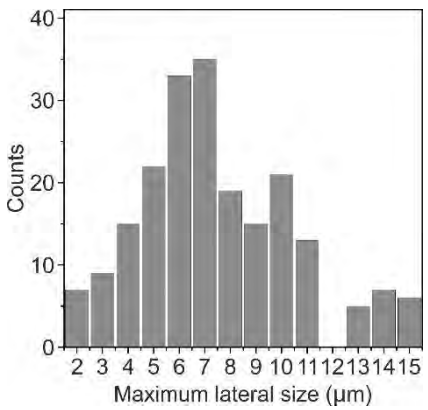

Figure S1. Histogram of the maximum lateral size distribution obtained from the as-grown VP films on the SiO_2/Si substrate.

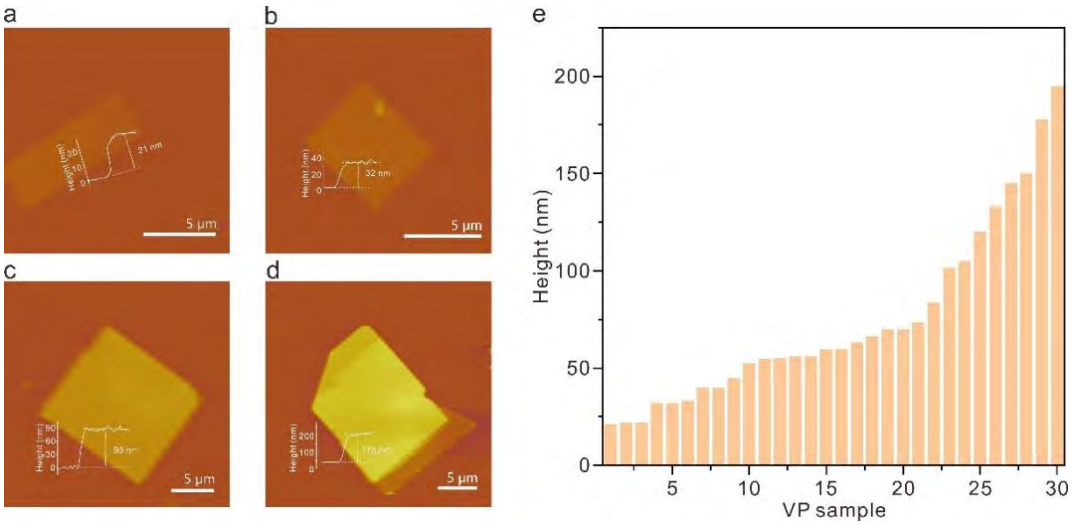

Figure S2. (a-d) AFM images and height profiles of the as-grown VP on SiO_2/Si substrate; (e) The height statistics from 30 randomly VP samples.

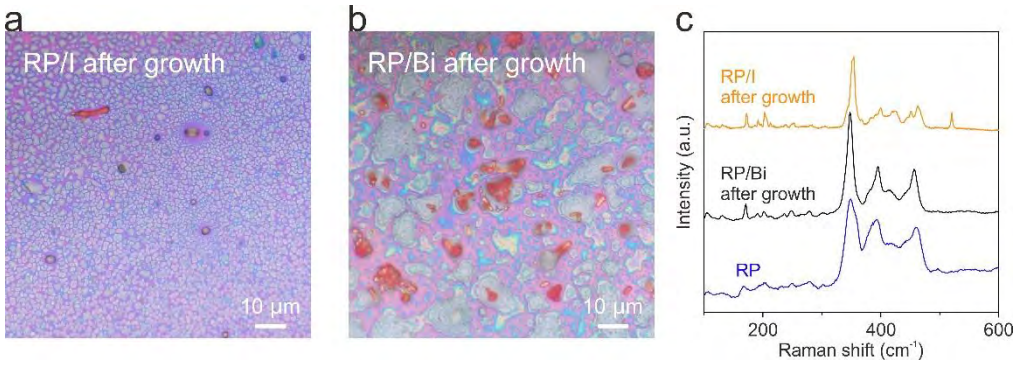

Figure S3. Contrast experiment of CVT growth without Bi or I: (a) Optical microscopy (OM) image after CVT growth without Bi; (b) OM image after CVT growth without I; (c) Raman scattering spectra of RP/I and RP/Bi after CVT growth and pristine RP.

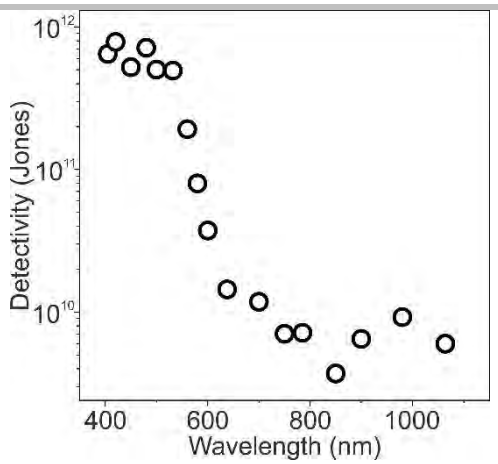

Figure S4. Measured specific detectivity (D_{M}^{*}) as a function of wavelength from visible to near-infrared with D_{M}^{*} obtained by $D_{M}^{*} = A^{1/2} / \mathrm{NEP}$ at a bias voltage of 5 V.

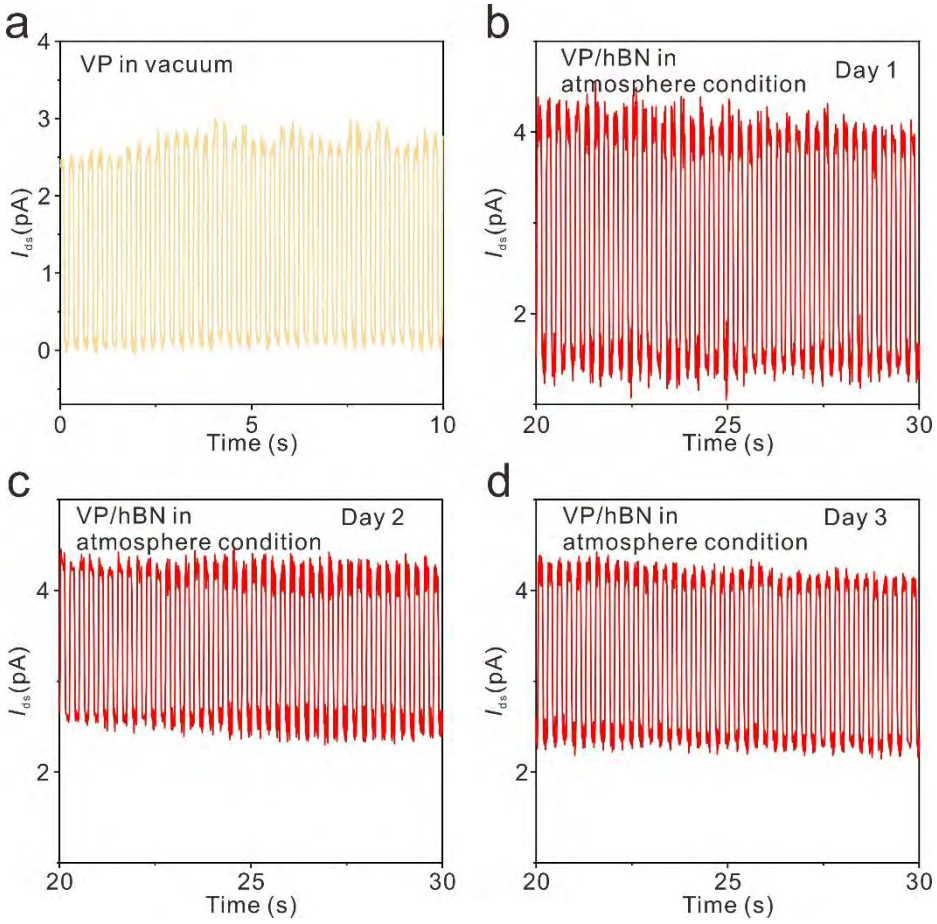

Figure S5. (a) Total currents I_{ds} as a function of time for VP in vacuum; (b-d) Total currents I_{ds} as a function of time for VP/hBN in atmosphere condition from one to three day. Above tests were under power density of 0.26 mW cm^{-2} and V_{ds} of 2.5 V.

Table S1. Photoelectric response and performance of 2D mateirls.

Materials	Resposivity (A/W)	Wavelength range	Time (ms)	D_C^* (Jones)	D_M^* (Jones)	Light source	Incidet Power	Power density (μW/cm^2)	Refs.
MoS_2	2570	Vis-NIR	1.8/2	2.2×10^{12}		Laser	1 nW	2×10^4	[1]
WS_2	5.2×10^{-3}	532 nm	1	4.9×10^9		Laser		70	[2]
WS_2	0.78	405 nm	7.8/37.2	4.9×10^{11}		Laser	0.1 μW	1×10^3	[3]
ReS_2	8.8×10^5	532 nm	$1\times10^4\times$	1.2×10^{12}		Laser	6 pW	760	[4]
In_2Se_3	9.8×10^4	405–940 nm	9×10^3	3.3×10^{13}		Laser	1 nW	3.18	[5]
SnSe	1.1×10^3	500–700 nm	14.5/8.1	1.0×10^{10}		Laser		6.3×10^3	[6]
PtS_2	1.6×10^3	500 nm	460/460	2.9×10^{11}		Not mentioned	97.6 μW	3.1×10^3	[7]
$PtSe_2$	4.5	Vis-MIR	1.1/1.2		7×10^8	Laser		5×10^4	[8]
$PdSe_2$	3.6	Vis-MIR			1.31×10^9	Laser		4.8×10^4	[9]
$InSiTe_3$	0.071	UV-NIR	0.013	7.59×10^9		Laser		63.4	[10]
BP	82	532–3390 nm				Laser	1.6 nW	1.7×10^3	[11]
Te	383	520–3390 nm	0.6			Laser	1 nW	1.2×10^5	[12]
SVP	12.5	Vis-NIR	3.82/3.03	1.38×10^{13}	6.4×10^{11}	Monochromatic halogen lamp	9.4 nW	0.3	This work

Table S2. The photoelectric performance of VP.

Materials	Resposivity (A/W)	Wavelength range	Time	D_C^* (Jones)	D_M^* (Jones)	Light source	Incidet Power	Power density (μW/cm^2)	Refs.
VP	0.01	300–690 nm	0.16/0.21 s			Laser			[13]
VP	6	250–800 nm	3.2 ms	2.0×10^{12}		Laser		0.1	[14]
Ar+ plasma treated VP	0.015	370–810 nm				Laser		29.2×10^3	[15]
$P_{20.56}Sb_{0.44}$	1×10^{-5}	Visble				Laser			[16]
VP/MoS_2	3.82×10^5	Visble	0.19/6.7 s	9.17×10^{13}		Laser	6×10^{-3} nW		[17]
SVP	12.5	Vis-NIR	3.82/3.03 ms	1.38×10^{13}	6.4×10^{11}	Monochromatic halogen lamp	9.4 nW	0.3	This work

References

[1] X. Wang, P. Wang, J. Wang, W. Hu, X. Zhou, N. Guo, H. Huang, S. Sun, H. Shen, T. Lin, M. Tang, L. Liao, A. Jiang, J. Sun, X. Meng, X. Chen, W. Lu, J. Chu, Ultrasensitive and Broadband MoS_2 Photodetector Driven by Ferroelectrics, *Adv. Mater.* **2015**, *27*, 6575-6581.

[2] C. Y. Lan, Z. Y. Zhou, Z. F. Zhou, C. Li, L. Shu, L. F. Shen, D. P. Li, R. T. Dong, S. P. Yip, J. Ho, Wafer-scale synthesis of monolayer WS_2 for high-performance flexible photodetectors by enhanced chemical vapor deposition, *Nano Res.* **2018**, *11*, 3371-3384.

[3] W. Gao, S. Zhang, F. Zhang, P. Wen, L. Zhang, Y. Sun, H. Chen, Z. Zheng, M. Yang, D. Luo, N. Huo, J. Li, 2D WS_2 Based Asymmetric Schottky Photodetector with High Performance, *Adv. Electron. Mater.* **2020**, *7*.

[4] E. F. Liu, M. S. Long, J. W. Zeng, W. Luo, Y. J. Wang, Y. M. Pan, W. Zhou, B. G. Wang, W. D. Hu, Z. H. Ni, Y. M. You, X. A. Zhang, S. Q. Qin, Y. Shi, K. Watanabe, T. Taniguchi, H. T. Yuan, H. Y. Hwang, Y. Cui, F. Miao, D. Y. Xing, High Responsivity Phototransistors Based on Few-Layer ReS_2 for Weak Signal Detection, *Adv. Funct. Mater.* **2016**, *26*, 1938-1944.

[5] J. O. Island, S. I. Blanter, M. Buscema, H. S. van der Zant, A. Castellanos-Gomez, Gate Controlled Photocurrent Generation Mechanisms in High-Gain In_2Se_3 Phototransistors, *Nano Lett.* **2015**, *15*, 7853-7858.

[6] X. Zhou, L. Gan, W. Tian, Q. Zhang, S. Jin, H. Li, Y. Bando, D. Golberg, T. Zhai, Ultrathin $SnSe_2$ Flakes Grown by Chemical Vapor Deposition for High-Performance Photodetectors, *Adv. Mater.* **2015**, *27*, 8035-8041.

[7] L. Li, W. K. Wang, Y. Chai, H. Q. Li, M. L. Tian, T. Y. Zhai, Few-Layered PtS_2 Phototransistor on h-BN with High Gain, *Adv. Funct. Mater.* **2017**, *27*, 1701011.

[8] X. Yu, P. Yu, D. Wu, B. Singh, Q. Zeng, H. Lin, W. Zhou, J. Lin, K. Suenaga, Z. Liu, Q. J. Wang, Atomically thin noble metal dichalcogenide: a broadband mid-infrared semiconductor, *Nat. Commun.* **2018**, *9*, 1545.

[9] Q. Liang, Q. Wang, Q. Zhang, J. Wei, S. X. Lim, R. Zhu, J. Hu, W. Wei, C. Lee, C. Sow, W. Zhang, A. T. S. Wee, High-Performance, Room Temperature, Ultra-Broadband Photodetectors Based on Air-Stable $PdSe_2$, *Adv. Mater.* **2019**, *31*, e1807609.

[10] J. Chen, L. Li, P. Gong, H. Zhang, S. Yin, M. Li, L. Wu, W. Gao, M. Long, L. Shan, F. Yan, G. Li, A Submicrosecond-Response Ultraviolet-Visible-Near-Infrared Broadband Photodetector Based on 2D Tellurosilicate $InSiTe_3$, *ACS Nano* **2022**, *16*, 7745-7754.

[11] Q. Guo, A. Pospischil, M. Bhuiyan, H. Jiang, H. Tian, D. Farmer, B. Deng, C. Li, S. J. Han, H.

Wang, Q. Xia, T. P. Ma, T. Mueller, F. Xia, Black Phosphorus Mid-Infrared Photodetectors with High Gain, *Nano Lett.* **2016**, *16*, 4648-4655.

[12] C. Shen, Y. Liu, J. Wu, C. Xu, D. Cui, Z. Li, Q. Liu, Y. Li, Y. Wang, X. Cao, H. Kumazoe, F. Shimojo, A. Krishnamoorthy, R. K. Kalia, A. Nakano, P. D. Vashishta, M. R. Amer, A. N. Abbas, H. Wang, W. Wu, C. Zhou, Tellurene Photodetector with High Gain and Wide Bandwidth, *ACS Nano* **2020**, *14*, 303-310.

[13] A. G. Ricciardulli, Y. Wang, S. Yang, P. Samorì, Two-Dimensional Violet Phosphorus: A p-Type Semiconductor for (Opto)electronics, *J. Am. Chem. Soc.* **2022**, *144*, 3660-3666.

[14] J. Xue, S. Wang, J. Zhou, Q. Li, Z. Zhou, Q. Hui, Y. Hu, Z. Zhou, Z. Feng, Q. Yan, Y. Yu, Y. Weng, R. Tang, X. Su, Y. Xin, F. Zheng, S. Ju, L. You, L. Fang, Passivating violet phosphorus against ambient degradation for highly sensitive and long-term stable optoelectronic devices, *Appl. Phys. Lett.* **2023**, *122,* 181903.

[15] Y. Li, S. Cai, W. K. Lai, C. Wang, L. Rogée, L. Zhuang, L. Zhai, S. Lin, M. Li, S. P. Lau, Impurity-Induced Robust Trionic Effect in Layered Violet Phosphorus, *Adv. Opt. Mater.* **2022**, *10*, 2101538.

[16] F. Baumer, Y. Ma, C. Shen, A. Zhang, L. Chen, Y. Liu, D. Pfister, T. Nilges, C. Zhou, Synthesis, Characterization, and Device Application of Antimony-Substituted Violet Phosphorus: A Layered Material, *ACS Nano* **2017**, *11*, 4105-4113.

[17] Y. Zhang, T. Zhu, N. Zhang, Y. Li, X. Li, M. Yan, Y. Tang, J. Zhang, M. Jiang, H. Xu, Air-Stable Violet Phosphorus/MoS_2 van der Waals Heterostructure for High-Responsivity and Gate-Tunable Photodetection, *Small* **2023**, *19*, 2301463.